nanomaterials

MDPI

Article

2D In-Plane CuS/Bi_2WO_6 p-n Heterostructures with Promoted Visible-Light-Driven Photo-Fenton Degradation Performance

Li Guo [1], Kailai Zhang [1], Xuanxuan Han [1], Qiang Zhao [1], Danjun Wang [1,2,*] and Feng Fu [1,*]

[1] College of Chemistry and Chemical Engineering, Shaanxi Key Laboratory of Chemical Reaction Engineering, Yan'an University, Yanan 716000, China

[2] State Key Laboratory of Organic-Inorganic Composites Beijing Key Laboratory of Electrochemical Process and Technology for Materials, Beijing University of Chemical Technology, Beijing 100029, China

* Correspondence: wangdanjun@yau.edu.cn (D.W.); fufeng@yau.edu.cn (F.F.)

Received: 29 June 2019; Accepted: 9 August 2019; Published: 11 August 2019

Abstract: Photo-Fenton degradation of pollutants in wastewater is an ideal choice for large scale practical applications. Herein, two-dimensional (2D) in-plane CuS/Bi_2WO_6 p-n heterostructures have been successfully constructed by an in situ assembly strategy and characterized using XRD, XPS, SEM/TEM, EDX, UV-Vis-DRS, PL, TR-PL, ESR, and VB-XPS techniques. The XPS and the TEM results confirm the formation of CuS/Bi_2WO_6 heterostructures. The as-constructed CuS/Bi_2WO_6 showed excellent absorption in visible region and superior charge carrier separation efficiency due to the formation of a type-II heterojunctions. Under visible light irradiation, 0.1% CuS/Bi_2WO_6 heterostructure exhibited the best photo-Fenton-like catalytic performance. The degradation efficiency of Rhodamine B (RhB, 20 mg·L^{-1}) can reach nearly 100% within 25 min, the apparent rate constant (k_{app}/min^{-1}) is approximately 40.06 and 3.87 times higher than that of pure CuS and Bi_2WO_6, respectively. The degradation efficiency of tetracycline hydrochloride (TC-HCl, 40mg·L^{-1}) can reach 73% in 50 min by employing 0.1% CuS/Bi_2WO_6 heterostructure as a photo-Fenton-like catalyst. The promoted photo-Fenton catalytic activity of CuS/Bi_2WO_6 p-n heterostructures is partly ascribed to its low carriers recombination rate. Importantly, CuS in CuS/Bi_2WO_6 heterostructures is conducive to the formation of heterogeneous photo-Fenton catalytic system, in which Bi_2WO_6 provides a strong reaction site for CuS to avoid the loss of Cu^{2+} in Fenton reaction, resulting in its excellent stability and reusability. The possible photo-Fenton-like catalytic degradation mechanism of RhB and TC-HCl was also elucidated on the basis of energy band structure analysis and radical scavenger experiments. The present study provides strong evidence for CuS/Bi_2WO_6 heterostructures to be used as promising candidates for photo-Fenton treatment of organic pollutants.

Keywords: Bi_2WO_6 nanosheets; photo-Fenton; degradation; visible light irradiation; 2D in-plane heterostructures

1. Introduction

In recent years, with the continuous development of modern economic society, the problem of water pollution is becoming more and more serious [1–3]. Especially organic dye and antibiotic wastewater discharged from factories have attracted people's attention [4–7]. The complex structure of the dye and antibiotic molecules containing amino groups, carboxyl groups, and benzene rings, lead to toxicity (teratogenic, carcinogenic, and mutagenic) and poor biodegradability [1–7]. If the dye and antibiotic-containing wastewaters are directly discharged into the freshwater without treatment, the human health and ecosystem will be threatened. Therefore, finding a simple, efficient, and low-cost water pollution remediation method has attracted the attention of researchers.

Among them, advanced oxidation processes (AOPs) have been regarded as promising methods for removing organic pollutants from wastewater, especially the photo-Fenton technology combined with the advantages of photocatalysis and Fenton catalysis, and have been greatly developed [8–13]. It is well known that the photo-Fenton technology is based on the enhanced electron transfer between H_2O_2 and iron, copper-based catalysts under light irradiation, and then cause high active free radicals such as ·OH to remove organic pollutants [14–18]. Moreover, the heterogeneous Fenton catalyst because of the low metal ion leaching amount, the wide pH application value, and excellent cycle performance has become a research hot spot, and has shown good application prospects [14–20].

Bi-based semiconductors such as Bi_2WO_6 have attracted much attention in the application of photocatalytic wastewater treatment, due to the suitable band gap energy, low cost, and better catalytic performance [21–24]. It has also been confirmed by combining an additional photocatalyst having a transitional metal oxidation state with Bi-based semiconductors to form heterogeneous photo-Fenton catalysts for pollutants treatment [25–27]. As one of the narrow-band gap Cu-based semiconductors with the advantages of being non-toxic, low-cost, and easy to access, CuS has been extensively studied in combination with other photocatalysts for photocatalytic or photo-Fenton degradation of organic pollutants [28–31]. For example, Gao et al. [28] reported that the introduction of CuS into TiO_2 by cysteine-assisted in situ synthesis is helpful for rapid transfer and separation of the carriers, thus improving photocatalytic activity. Cai et al. [29] used an in situ synthesis technique to prepare g-C_3N_4/CuS p-n heterostructured photocatalyst. The presence of CuS in heterostructure improves the optical absorption and also efficiently facilitates the separation of photo-generated electron–hole pairs. In addition, Bhoi et al. [30] reported that $BiFeO_3$ was modified by CuS nanorods through a two-step process to generate a type-II heterostructure, which can enhance the photo-Fenton catalytic activity of $BiFeO_3$, resulting from enhanced visible light absorption, greater charge carrier separation, and improved charge mobility. A similar phenomenon has also been observed on CuS/$Bi_2W_2O_9$ heterojunctions by Bhoi's group [31]. Under the action of photogenerated electrons, the circulation of Cu^+ and Cu^{2+} on the surface of photocatalyst can significantly promote the photo-Fenton process, which can produce ·OH more effectively than the traditional Fenton reaction, and ultimately improve the photo-Fenton performance [32].

In this paper, we synthesized CuS/Bi_2WO_6 heterostructure by a simple two-step hydrothermal method. The activity results show that the heterostructures can greatly promote photo-generated electron–hole separation, and the photo-Fenton catalytic activity of degradation of Rhodamine B (RhB) and tetracycline hydrochloride (TC-HCl) is significantly improved. In addition, the composition of the heterogeneous Fenton reaction system can significantly improve the recyclability of the catalyst. Moreover, we have investigated the effects of H_2O_2 concentration, catalyst dosage, and initial pH value on the photo-Fenton activity, and detailed the possible mechanism of photo-Fenton catalytic reaction.

2. Experimental Section

2.1. Chemicals

Sodium hydroxide (NaOH, 96.0%) and cetyltrimethylammonium bromide (CTAB, $C_{19}H_{42}BrN$, 99.0%) were purchased from Tianjin Kemiou Chemical Reagent Co., Ltd. (Tianjin, China). Sodium tungstate dihydrate ($Na_2WO_4{\cdot}2H_2O$, 99.5%), bismuth nitrate pentahydrate ($Bi(NO_3)_3{\cdot}5H_2O$, 99%), and absolute alcohol (C_2H_5OH, 99.7%) were purchased from Tianjin Zhiyuan Chemical Reagent Co., Ltd. (Tianjin, China). Hydrochloric acid (HCl, 36%), nitric acid (HNO_3, 63%) and ammonia solution ($NH_3{\cdot}H_2O$, 28%) were purchased form Sichuan Xilong chemical Co., Ltd. (Sichuan, China). Thiourea (CH_4N_2S, 99.0%) was purchased from Sinopharm Chemical Reagent Co., Ltd (Shanghai, China). Copper nitrate trihydrate ($Cu(NO_3)_2{\cdot}3H_2O$, 99.0%) was bought from Tianjin Yongsheng Fine Chemical Co., Ltd. (Tianjin, China). The deionized water was used as a solvent. All the reagents were of analytical grade and were used without any further purification.

2.2. Sample Preparation

2.2.1. Preparation of Bi_2WO_6 Nanosheets

The Bi_2WO_6 nanosheets were synthesized by a modified hydrothermal method in accordance with previous report [33]. First, 1.94 g of $Bi(NO_3)_3{\cdot}5H_2O$ was dissolved into 5 mL of 4 mol·L^{-1} HNO_3 aqueous solution. To this solution, 0.02 g of cetyltrimethylammonium bromide (CTAB) and 0.60 g of $Na_2WO_4{\cdot}2H_2O$ in 50 mL of deionized water was then slowly added dropwise to the above solution under magnetic stirring, and the solution of pH is adjusted to neutral with 1:1 concentrated ammonia water ($NH_3{\cdot}H_2O$), and finally stirred vigorously for 1 h to obtain a white precipitate. The whole mixture was transferred to a 100 mL Teflon-lined stainless steel autoclave and treated hydrothermally at 180 °C for 14 h. After cooling to room temperature, it was washed three times with deionized water and absolute ethanol, dried at 70 °C for 8 h, and calcined at 300 °C for 3 h in a muffle furnace to remove the surface residue.

2.2.2. Preparation of CuS/Bi_2WO_6 Heterostructure

The CuS/Bi_2WO_6 composites were synthesized by a hydrothermal method according to the previous literature with minor revision [31]. In brief, (0.0024 g, 0.0315 mmol) of thiourea was dissolved in 75 mL water, then 1 g of as-prepared Bi_2WO_6 was added under ultrasonication for 10 min. Subsequently, (0.0025 g, 0.0103 mmol) of $Cu(NO_3)_2{\cdot}3H_2O$ was added with another ultrasonication for 10 min. After stirring for 1 h, the resulting suspension were placed in a 100 mL stainless steel autoclave at 150 °C for 24 h. Finally, when the oven was naturally cooled to room temperature, the obtained products were separated by centrifugation and washed 3 times with deionized water and absolute ethanol, and dried at 70 °C in vacuum overnight to obtain 0.1% CuS/Bi_2WO_6 composite (Herein, 0.1% represents the weight ratio of CuS to Bi_2WO_6). Following the similar procedure, a series of X% CuS/Bi_2WO_6 (X = 0.02%, 0.5%, 1% and 2%) heterostructures were prepared using the same procedure, only the amount of $Cu(NO_3)_2{\cdot}3H_2O$ and thiourea was changed. For comparison, pure CuS was also prepared by the same procedure in the absence of Bi_2WO_6.

2.3. Characterization

The XRD patterns of samples were recorded by a Shimadzu XRD-7000 using a Ni filtered Cu Kα (λ = 0.15418 nm) as X-ray source. The XRD data was obtained in 2θ range of 10–80° at a scan rate of 8°·min^{-1}. The X-ray photoelectron spectra (XPS) patterns of samples were measured on a PHI-5400 (Physical Electronics PHI, MN, America) 250 xi system with Al Kα X-rays as the excitation source. The morphology and microscopic size of the samples were carried out by a JSM-6700F (Japan electronics) and a (JEM-2100) (Japan electronics). Energy disperse X-ray (EDX) analysis was performed on a field emission scanning electron microscope (JSM-7610F). The optical properties of the samples were detected on a UV-2550 spectrophotometer (Japan Shimadzu, Kyoto, Japan) within 200 nm to 800 nm, using BaSO4 as a reflectance standard. The photoluminescence (PL) spectra of samples were conducted on a F-4600 spectrophotometer (Hitachi, Japan). Time-resolved photoluminescence (TR-PL) spectra were conducted on a FLS920 fluorescence spectrometer (Edinburgh Analytical Instruments, Edinburgh, UK). The electron spin resonance (ESR) spectra were obtained on a JES-FA300 model spectrometer (ESR, Japan JEOL, Tokyo, Japan) under visible light irradiation (λ ≥ 420 nm). The magnetic central field intensity, scanning width, scanning time, and microwave power are 324.006 mT, 10.00 mT, 60 s, and 0.99800 mW, respectively. The spectra is 4096 points. In a typical experiment for ·OH detection, 10 mg of photocatalyst was dispersed in the mixture solution of 20 mL of ultrapure water and 50 μL of H_2O_2 under ultrasonic for 30 min. Then, 10 μL of mixture was sampled and 10 μL of 5,5-dimethyl-1-pyrroline-N-oxide (DMPO) (10 ppm) was added with ultrasonic dispersion for 5 min. Thereafter, the obtained mixtures were sampled by a capillary tube and placed into a quartz ESR tube then subjected to test. The signals were collected after visible light irradiation for different time. Following a similar process—just replacing ultrapure water with methanol—·O_2^- was also detected.

2.4. Photocatalytic and Photo-Fenton Catalytic Activity Measurement

The prepared samples were used as photo and photo-Fenton like catalysts for the degradation of Rhodamine B (RhB, 20 mg·L^{-1}) and tetracycline hydrochloride (TC-HCl, 40 mg·L^{-1}). The photocatalytic degradation experiments were carried in photocatalytic reactor (Xujiang Mechanical and Electrical Factory, Nanjing, China, XPA-7). A 300 W metal halide lamp equipped with a 420 nm cut-off filter was used to simulate visible light source. The circulating cooling water was introduced to avoid liquid volatilization and keep the reaction temperature at 25 °C through the temperature control system. Moreover, 0.02 g of the catalyst was added to a 50 mL capacity reactor containing 20 mL of simulated contaminants aqueous solution adjusting with the determined pH (with NaOH or HCl aqueous solution), and then stirred under dark conditions for 2 h to ensure adsorption/desorption equilibrium, then a certain volume of H_2O_2 (30%) was added when the light source was turned on. At a certain interval, 2 mL of the supernatant was removed for centrifugation, and then the maximum characteristic absorption peaks of RhB and TC-HCl at 554 nm and 357 nm were measured by UV-Vis spectroscopy (Shimadzu UV-2550), respectively.

3. Results and Discussion

3.1. Structure, Composition, and Morphology of Samples

The XRD patterns of as-synthesized Bi_2WO_6, CuS, and CuS/Bi_2WO_6 samples are shown in Figure 1. For the Bi_2WO_6 sample, all the diffraction peaks can be assigned to the orthorhombic phase Bi_2WO_6 (JCPDS No. 39-0256) [34]. Besides this, the peaks observed for pure CuS are assigned to hexagonal covellite phase (JCPDS No.06-0464) [31]. For the 0.1% CuS/Bi_2WO_6 heterostructure, the characteristic peaks of Bi_2WO_6 are still retained, but there no characteristic peaks of CuS species and other phases appear in the XRD pattern, owing to the low loading amount of CuS.

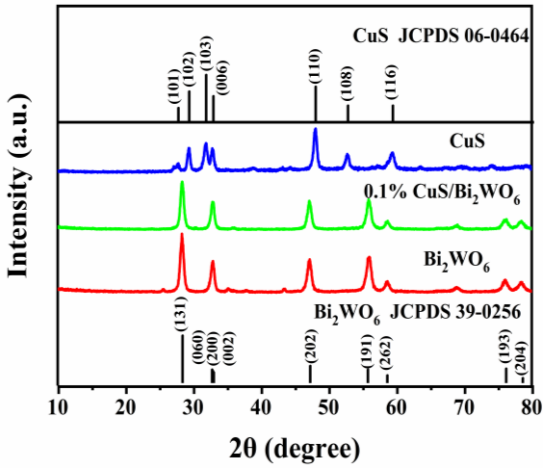

Figure 1. XRD patterns of the CuS, Bi_2WO_6 nanosheets and 0.1% CuS/Bi_2WO_6 heterostructure.

To ulteriorly investigate the surface composition and chemical state information of the CuS/Bi_2WO_6 heterostructure, XPS measurement was subsequently performed, and the binding energy of C 1s was calibrated at 284.6 eV. The surface survey spectrum (Figure 2a) showed the existence of Bi, W, and O elements in both the Bi_2WO_6 and 0.1% CuS/Bi_2WO_6 heterostructure, and exemplified only the existence of Cu, S, and C elements in the CuS, in which the binding energy of C 1s is ascribed to the adventitious carbon from the XPS instrument itself. The high-resolution spectra of Bi 4f, W 4f, Cu 2p, and S 2p are shown in Figure 2b–e, respectively. Figure 2b shows two peaks of 0.1% CuS/Bi_2WO_6 heterostructure are observed at around 164.57 and 159.25 eV, corresponding to the Bi $4f_{5/2}$ and Bi $4f_{7/2}$ energy states of Bi^{3+} [35]. The strong peaks at 37.48 and 35.49 eV are assigned to the W $4f_{5/2}$ and W $4f_{7/2}$ for W^{6+} (Figure 2c) [36]. The corresponding Cu 2p peaks are located at 952.42 and 932.02 eV, and

are designated Cu^{2+} $2p_{1/2}$ and Cu^{2+} $2p_{3/2}$ (Figure 2d) [30,31,37]. It is important to note that the binding energies of Bi 4f, W 4f, and Cu 2p in the 0.1% CuS/Bi_2WO_6 heterostructure all exhibited slight shift to the binding energy compared with that of Bi_2WO_6 or CuS (Figure 2b–d) due to the interaction between CuS and Bi_2WO_6 nanosheets. As for S 2p, it can be seen that the standard peaks of CuS at 163.4 eV and 162.4 eV for S $2p_{1/2}$ and S $2p_{3/2}$ were observed, which are consistent with the reported binding energies in metal sulfide. (Figure 2e) [38]. On the contrary, two different peaks are unexpectedly similar to the binding energies of Bi^{3+} at 159.10 and 164.30 eV in the 0.1% CuS/Bi_2WO_6 heterostructure (Figure 2e). It may be because the binding energy of S^{2-} is very similar to that of Bi^{3+} [39]. The XRD and XPS results implied that 0.1% CuS/Bi_2WO_6 heterostructure was authentically obtained.

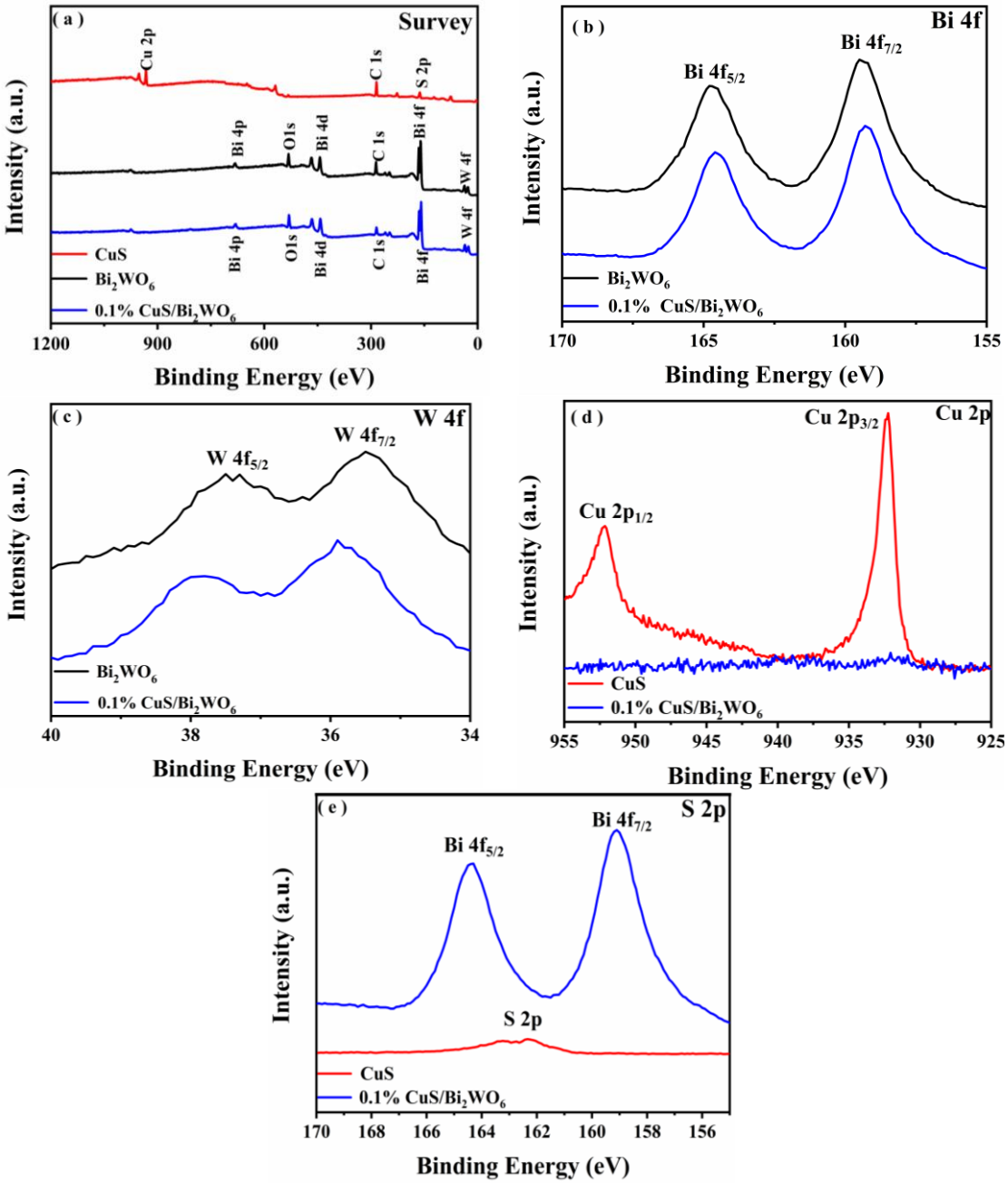

Figure 2. (**a**) The XPS survey spectra of Bi_2WO_6, CuS, and 0.1% CuS/Bi_2WO_6 heterostructure (**b**–**e**) High resolution XPS spectra of the Bi_2WO_6, CuS, and 0.1% CuS/Bi_2WO_6 heterostructure.

The morphology and size of the as-synthesized Bi_2WO_6, CuS, and 0.1% CuS/Bi_2WO_6 heterostructure were observed by SEM and TEM images. Figure 3a,b depict the nanosheet structures of Bi_2WO_6 with the average thickness of about 20 nm. Figure 3c,d show the SEM image of CuS sample presenting spherical-shape morphology assembled by uniform nanosheets with thickness of approximately 50 nm. As can be seen from Figure 3e,f, the CuS nanosheets were well in-plate assembled on the Bi_2WO_6 nanosheets, and the tight interfaces between Bi_2WO_6 and CuS further confirmed the formation of CuS/Bi_2WO_6 heterojunctions. Moreover, the energy-dispersive X-ray analysis of 0.1% CuS/Bi_2WO_6 heterostructure was shown in Figure 3g–l, which confirms the uniform distribution of Bi, W, O, Cu, and S species over the 0.1% CuS/Bi_2WO_6 heterostructure.

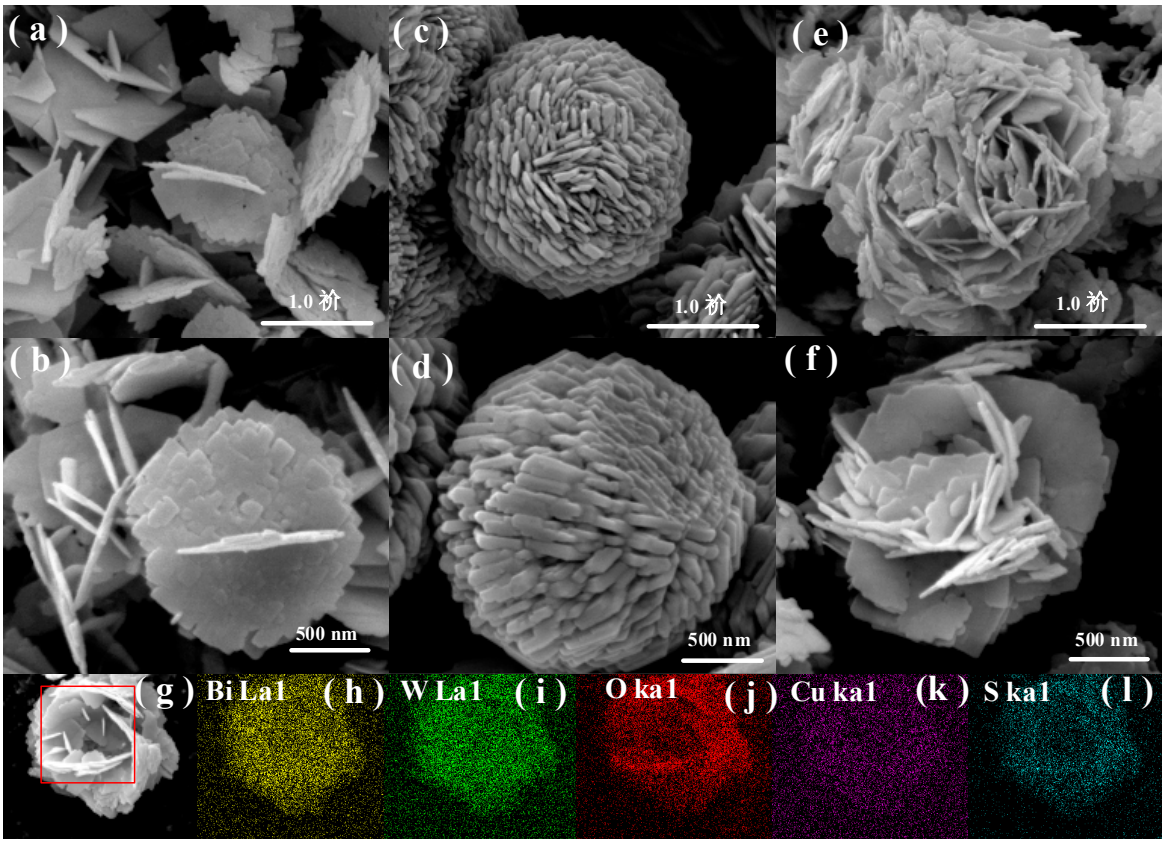

Figure 3. FESEM images of (**a**,**b**) Bi_2WO_6, (**c**,**d**) CuS, and (**e**,**f**) 0.1% CuS/Bi_2WO_6 heterostructure, and energy filtered elemental mapping of 0.1% CuS/Bi_2WO_6 heterostructure (**g**–**l**).

Figure 4a shows the in situ assembly strategy of 2D/2D CuS/Bi_2WO_6 heterostructures, which depicts the formation of CuS nanosheets onto Bi_2WO_6 nanosheets for assembling in-plane heterostructures. Figure 4b–d shows the TEM images of Bi_2WO_6, CuS and 0.1% CuS/Bi_2WO_6 composite. The TEM results further validated the nanosheet structures of Bi_2WO_6 and the microsphere structure of CuS assembled by nanosheets. The CuS and Bi_2WO_6 containing in 0.1% CuS/Bi_2WO_6 heterostructure were verified by HRTEM, as shown in Figure 4e. The lattice fringe spacing between adjacent crystal faces is 0.273 nm and 0.189 nm, which can be attributed to the (200) and (110) crystal plane of Bi_2WO_6 phase and CuS phase, respectively [40,41], leading to the formation of heterojunction.

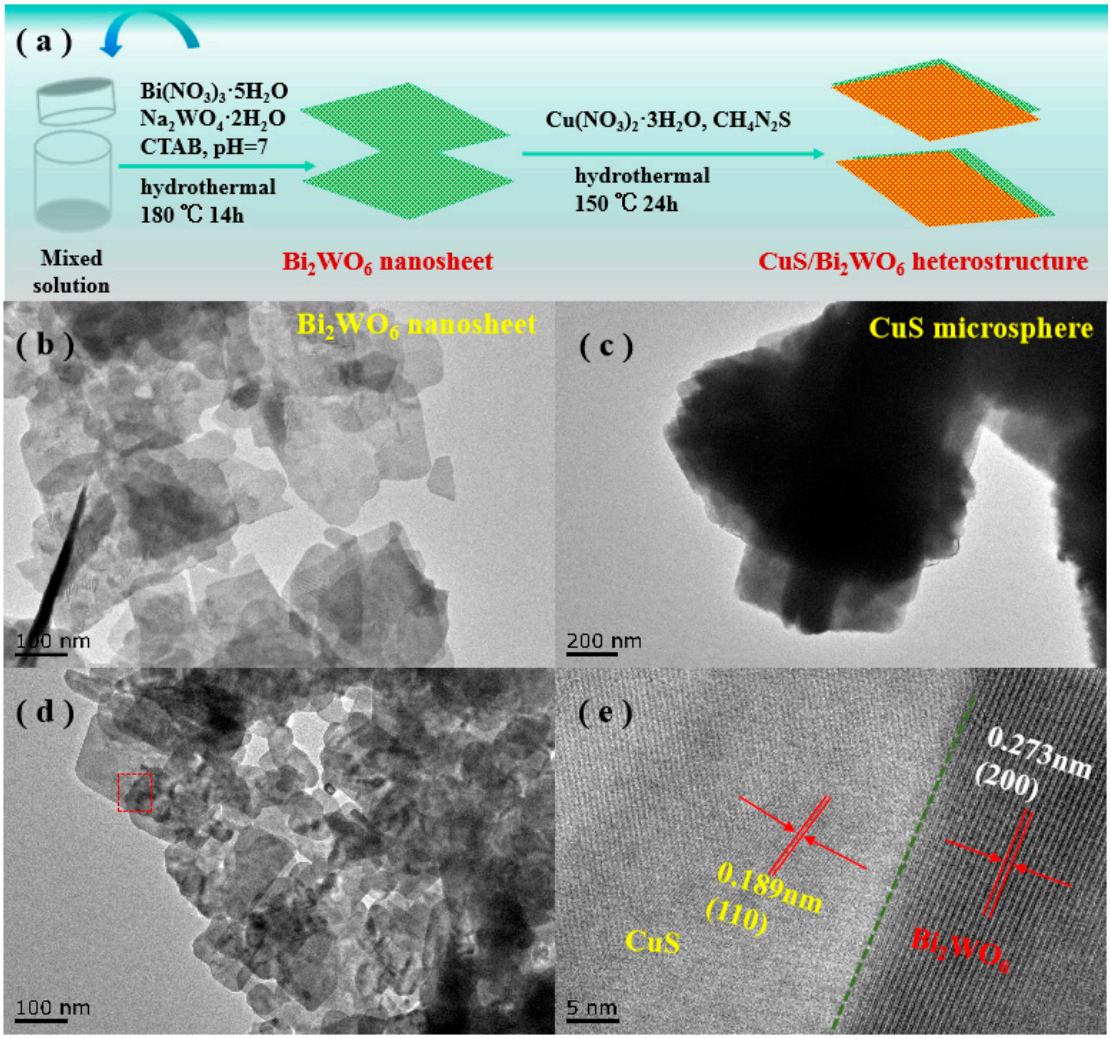

Figure 4. (**a**) Schematic preparation of CuS/Bi_2WO_6 sheet-onto-sheet p-n heterostructures. (**b**) TEM images of Bi_2WO_6. (**c**) TEM images of CuS. (**d**) TEM and (**e**) HRTEM image of as-prepared 2D/2D 0.1% CuS/Bi_2WO_6 sheet-onto-sheet heterostructure.

3.2. Photocatalytic and Photo-Fenton Catalytic Performance

The photo-Fenton and photocatalytic degradation of organic pollutants are shown in Figure 5. As can be seen from Figure 5a, the concentration of initial RhB hardly changes without catalyst, which fully proves the stability of its own molecules. However, after the addition of H_2O_2 alone, the degradation rate of RhB can reach 14%. In addition, compared to pure Bi_2WO_6, the loading of CuS slightly decreased its photocatalytic activity, which may be due to CuS covering up the active sites, eventually resulting in a decrease in activity.

As can be seen from Figure 5b, RhB was only degraded by 10% when CuS is added as a catalyst alone, which may be due to its high electron–hole recombination rate as a photo-Fenton catalyst. It is important to note that the degradation performance of RhB by photo-Fenton process over CuS/Bi_2WO_6 heterostructures is obviously enhanced. The as-prepared 0.1% CuS/Bi_2WO_6 heterostructure represents the optimal amount relative to photo-Fenton activity. Figure 5c shows that the rate constant implemented by the equation ln (C_0/C) = k_{app}·t, where k_{app}/min^{-1} means the apparent rate constant. The degradation efficiency of RhB (20 mg·L^{-1}) can reach nearly 100% within 25 min, the apparent rate constant (k_{app}/min^{-1}) is approximately 40.06 times and 3.87 times higher than that of pure CuS and Bi_2WO_6, respectively (Figure 5d). Hence, it can be concluded that loading CuS nanosheets on Bi_2WO_6 nanosheets can remarkably promote photo-Fenton catalytic performance.

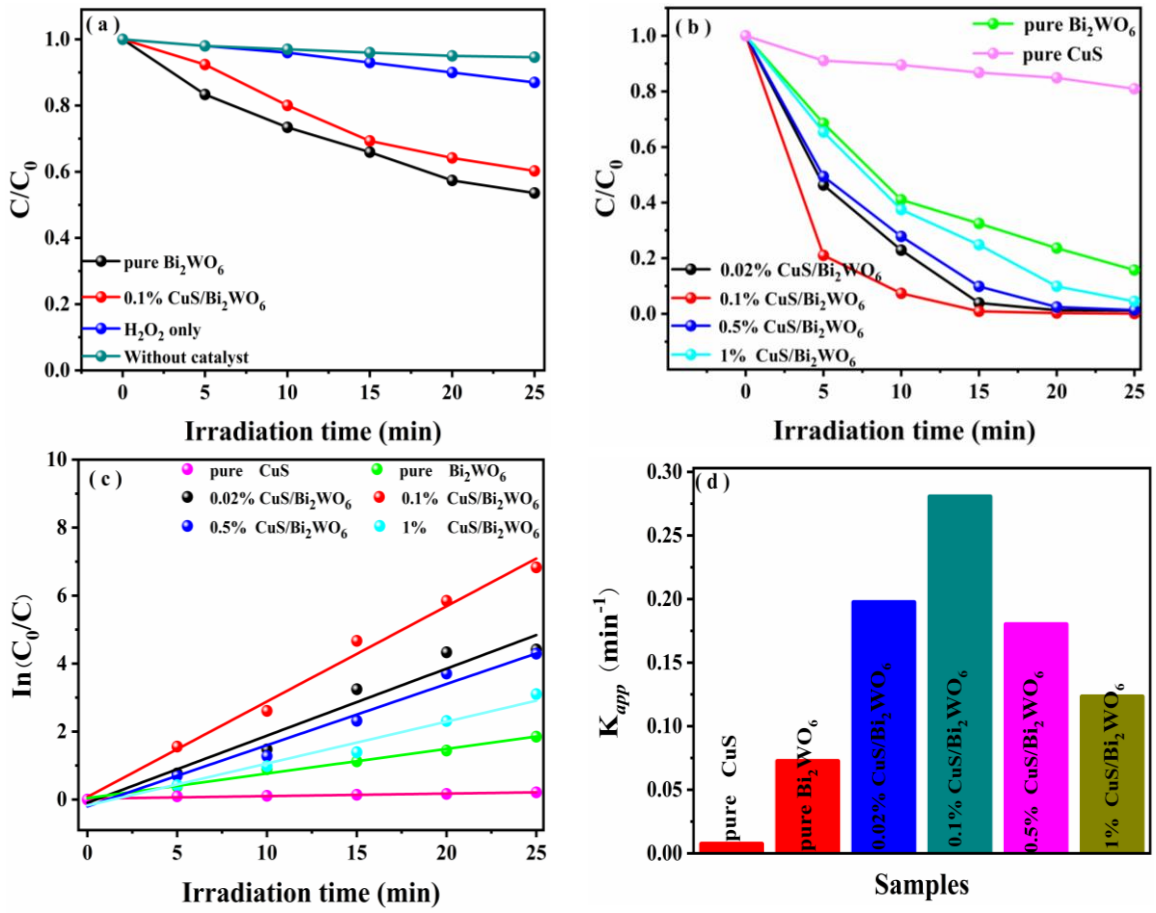

Figure 5. (**a**) The photo-catalytic degradation dynamic curves of RhB in the presence of pure Bi_2WO_6, H_2O_2 only, without catalyst, and 0.1% CuS/Bi_2WO_6 heterostructure. (Reaction conditions: T = 25 °C, concentration of RhB = 20 mg·L^{-1}, and catalyst concentration = 1 g·L^{-1}). (**b**) The photo-Fenton catalytic degradation dynamic curves of RhB in the presence of pure Bi_2WO_6, CuS, and a series of CuS/Bi_2WO_6 heterostructures. (Reaction conditions: T = 25 °C, the dosage of H_2O_2 = 100 μL, concentration of RhB = 20 mg·L^{-1}, and catalyst concentration = 1 g·L^{-1}). (**c**) The pseudo-first-order reaction kinetics and (**d**) values of reaction rate constants over the synthesized samples in the photo-Fenton reaction.

In order to show that the catalyst can handle a wide variety of wastewaters, the photocatalytic and photo-Fenton catalytic activity of the CuS/Bi_2WO_6 heterostructures in TC-HCl aqueous solution were also investigated. Figure 6a shows the variation of TC-HCl concentration of the degradation in different samples. It can be seen the photocatalytic effect of the 0.1% CuS/Bi_2WO_6 heterostructure is lower than that of pure Bi_2WO_6, which is the same as the activity of the comparison of the dye. At the same time, it is noted in Figure 6b that after the H_2O_2 is added, the photo-Fenton catalytic degradation efficiency was close to 73% in 50 min through the constructed 0.1% CuS/Bi_2WO_6 photo-Fenton system, which was obviously better than pure Bi_2WO_6.

We further explored the effect of H_2O_2 concentration, catalyst dosage, and initial pH value on the degradation performance of TC-HCl by 0.1% CuS/Bi_2WO_6 heterostructure under visible light irradiation. Firstly, the effect of different H_2O_2 concentrations on the degradation of TC-HCl is shown in Figure 7a. As the initial H_2O_2 concentration increased from 50 μL to 100 μL, the degradation efficiency increased gradually from 68.1% to 72.8%, while the initial H_2O_2 concentration further increased from 100 μL to 200 μL, the degradation efficiency increased slightly. From an economic point of view, the optimal concentration of H_2O_2 was chosen as 100 μL. This indicates that adding the appropriate amount of H_2O_2 is advantageous for increasing the photo-Fenton catalytic activity. Secondly, the effect of the catalyst dosage on the degradation of TC-HCl is shown in Figure 7b. It can be seen that there

is an optimum amount of catalyst and the photo-Fenton activity is highest at this time. When the optimum amount is exceeded, the activity is gradually decreased, which may be because too much catalyst blocks the light, and it eventually leads to a decrease in photo-Fenton catalytic activity. Finally, the effect of pH on the degradation of TC-HCl is shown in Figure 7c. As the pH increased from 5 to 7, the degradation efficiency of TC-HCl increased, and then continued to increase pH to 9, and the degradation activity declined instead, which indicated that it has better photo-Fenton activity under natural pH conditions. This is because under natural conditions, the photo-Fenton reaction is more likely to generate enough active free radicals to degrade pollutants.

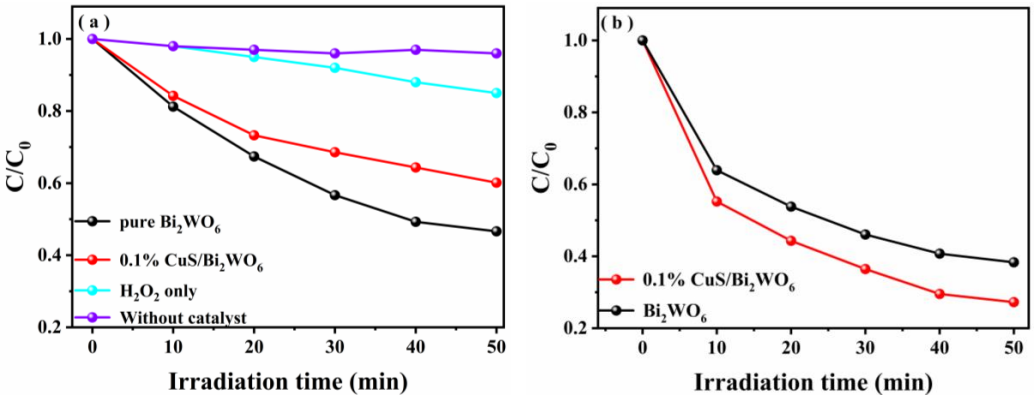

Figure 6. (**a**) The photo-catalytic degradation dynamic curves of TC-HCl in the presence of pure Bi_2WO_6, H_2O_2 only, without catalyst, and 0.1% CuS/Bi_2WO_6 heterostructure. (Reaction conditions: T = 25 °C, concentration of TC-HCl = 40 mg·L^{-1}, and catalyst concentration = 1 g·L^{-1}). (**b**) The photo-Fenton catalytic degradation dynamic curves of TC-HCl in the presence of pure Bi_2WO_6 and 0.1% CuS/Bi_2WO_6 heterostructure (Reaction conditions: T = 25 °C, the dosage of H_2O_2 = 100 μL, concentration of TC-HCl = 40 mg·L^{-1}, and catalyst concentration = 1 g·L^{-1}).

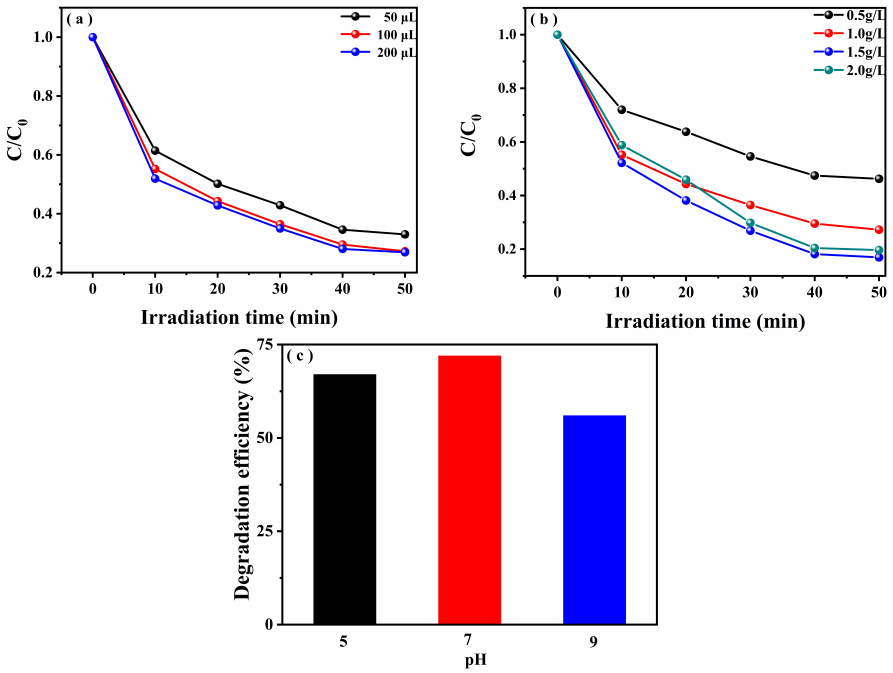

Figure 7. Effects of H_2O_2 concentration (**a**), catalyst dosage (**b**) and initial pH value (**c**) on the photo-Fenton catalytic activity for TC-HCl removal.

The cyclic experiments of TC-HCl were also carried out four times over 0.1% CuS/Bi_2WO_6 heterostructure (Figure 8a). It can be seen that the catalyst still maintains a high degradation efficiency after each cycle. Figure 8b presents the XRD patterns of fresh and reused 0.1% CuS/Bi_2WO_6 heterostructure in the photo-Fenton reaction. No impurity peaks were presented and only the peak intensity slightly decreased, which suggested that the catalyst has relatively stability. This showed that Cu^{2+} leaching problem in the traditional homogeneous Fenton reaction can be significantly restrained by employing CuS/Bi_2WO_6 heterostructures. According to the above results, the 0.1% CuS/Bi_2WO_6 heterostructure exhibited significantly enhanced catalytic performance compared with the previously reported catalysts for the degradation of dyes and antibiotics (Table 1), for instance, Bi_2WO_6/Fe_3O_4 [27], g-C_3N_4/CuS [29], TiO_2/Fe_3O_4 [42], etc. This comparison clearly reveals that the 0.1% CuS/Bi_2WO_6 heterostructure is a potential candidate for treating dye and antibiotic wastewater under visible light irradiation.

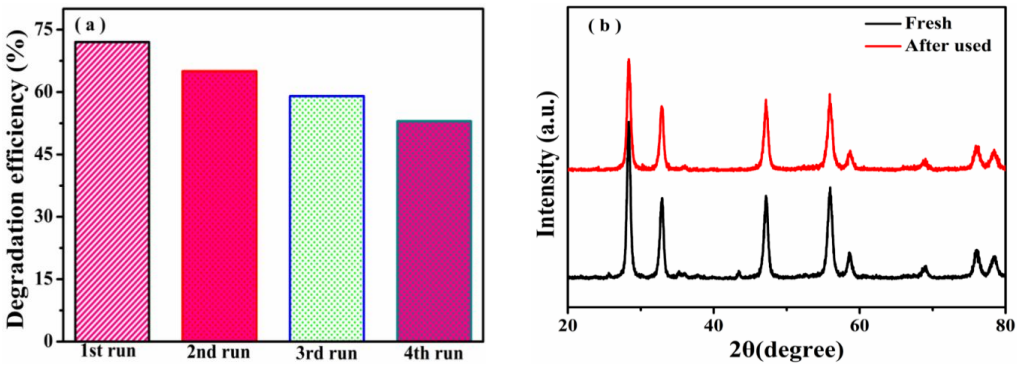

Figure 8. (**a**) Degradation efficiency of TC-HCl during different cycles, (Reaction conditions: initial pH value = 7, T = 25 °C, initial H_2O_2 concentration = 100 μL, concentration of TC-HCl = 40 mg·L^{-1}, and catalyst dosage = 1 g·L^{-1}); (**b**) XRD patterns of 0.1% CuS/Bi_2WO_6 heterostructure before and after photo-Fenton reaction.

3.3. Photocatalytic and Photo-Fenton Catalytic Mechanism

Figure 9 shows the UV−Vis DRS spectra of Bi_2WO_6, CuS and 0.1% CuS/Bi_2WO_6 heterostructure. Obviously, CuS exhibits a stronger absorption band in visible region, while Bi_2WO_6 exhibits weak absorption in visible region. After assembling CuS nanosheets on the surface of Bi_2WO_6 nanosheets, the absorption of visible region by the composite catalyst was slightly enhanced. Nevertheless, when light and H_2O_2 were simultaneously introduced, the heterogeneous photo-Fenton system formed by CuS and Bi_2WO_6 exhibited higher catalytic performance in the case of extremely low Cu^{2+} loading.

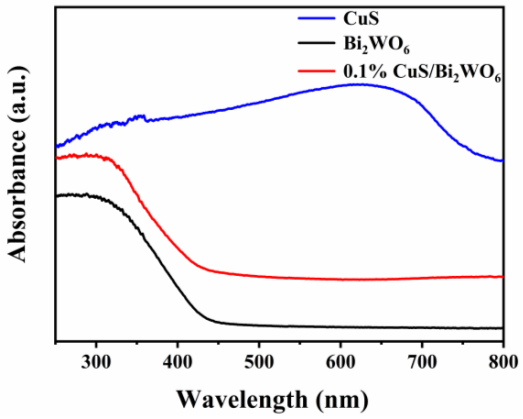

Figure 9. UV-Vis DRS spectrum of Bi_2WO_6, CuS, and 0.1% CuS/Bi_2WO_6 heterostructure.

Table 1. Comparison of photo and photo-Fenton catalytic performance for removal of pollutants.

Samples	Light Source		Organic Pollutants		Experimental Conditions				$\eta^{d)}$ (%)	Refs.
	Type [a)]	Power (W)	Type	Conc. [b)] ($mg \cdot L^{-1}$)	Catalyst (g/L)	t [c)] (time)	pH	H_2O_2		
Co_3O_4/Bi_2WO_6	Tungsten lamp	100	Methylene blue (MB)	10	1	80	8	1.96 mM	96	[26]
Bi_2WO_6/Fe_3O_4	Xe lamp	350	RhB	10	0.5	120	7	10 mM	95	[27]
CuS-TiO_2	Xe lamp	350	MB	10	1	180	-	-	100	[28]
g-C_3N_4/CuS	Xe lamp	300	RhB	10	0.3	60	-	-	96.8	[29]
CuS/$Bi_2W_2O_9$	Xe lamp	150	Diuron	10	0.75	180	-	200 μL	95	[31]
CuS/$Bi_4Ti_3O_{12}$	Xe lamp	250	2-methyl-4-chlorophenoxyacetic acid	10	0.25	180	-	150 μL	96	[41]
TiO_2/Fe_3O_4	UVC-lamp	10	TC-HCl	50	0.3	60	7	10 mM	98	[42]
0.1% CuS/Bi_2WO_6	Metal halide lamp	300	RhB	20	1.0	25	-	100 μL	100	this work
			TC-HCl	40	1.0	50	7		73	

[a)] UVC-lamp were the UV-light sources, Xe lamp, tungsten lamp and metal halide lamp were the visible-light source; [b)] concentration of pollutants; [c)] irradiation time; [d)] the total removal efficiency of organic pollutant.

The recombination rate of photogenerated electrons and holes of the materials were analyzed by photoluminescence (PL) spectroscopy. In general, the weak fluorescence intensity of the samples indicates that the recombination rate of photogenerated electrons and holes in the material is relatively low. It can be seen from Figure 10a that the Bi_2WO_6 has a higher recombination rate of photogenerated electrons and holes than other samples. The intensity of the diffraction peak of the 0.1% CuS/Bi_2WO_6 heterostructure is much lower than that of the Bi_2WO_6 alone, suggesting that the combination of Bi_2WO_6 and CuS can effectively inhibit the recombination of electrons and holes. This is beneficial for the photo-Fenton catalytic reaction involving H_2O_2. The time-resolved photoluminescence (TR-PL) spectroscopy of Bi_2WO_6 and 0.1% CuS/Bi_2WO_6 heterostructure are also used to detect the carrier lifetime, and the results were shown in Figure 10b. The photoelectron lifetimes conform to the two-exponential decay model. Decay times (τ_1 and τ_2) and PL aptitudes (A_1 and A_2) are given in Table 2. Compared to the Bi_2WO_6 (0.903 ns), the photogenerated charge carriers lifetime of 0.1% CuS/Bi_2WO_6 heterostructure is significantly prolonged (1.360 ns). The increased carriers lifetime can effectively promote the cycle of Cu^{2+} to Cu^{+}, and then Cu^{+} can react with H_2O_2 to generate ·OH with strong oxidation performance, thus improving the photo-Fenton catalytic performance.

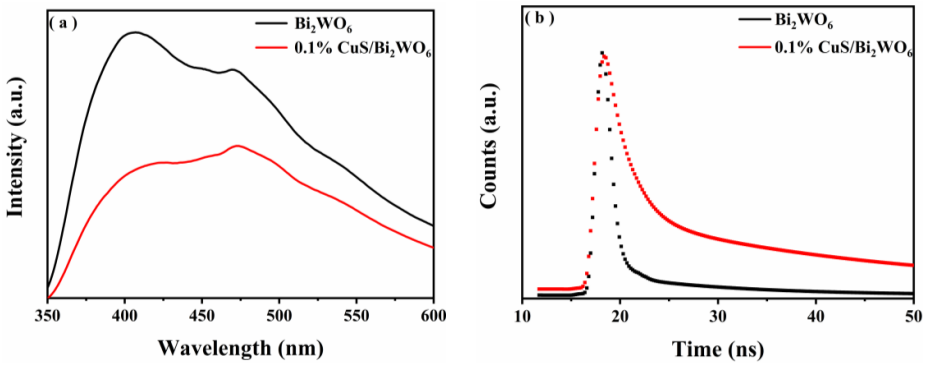

Figure 10. Photoluminescence (PL) spectra of Bi_2WO_6 and 0.1% CuS/Bi_2WO_6 heterostructure (**a**), time-resolved transient PL decay curves of Bi_2WO_6 and 0.1% CuS/Bi_2WO_6 heterostructure (**b**).

Table 2. Parameter of time-resolved PL decay curves.

Samples	τ_1 (ns)	A_1	τ_2 (ns)	A_2	T_{av} (ns)
Bi_2WO_6 nanosheets	0.903	2.22×10^{11}	12.205	1022.997	0.903
0.1% CuS/Bi_2WO_6	17.552	1.50×10^{3}	1.359	1.32×10^{9}	1.360

To investigate the catalytic mechanism, an in situ ESR study was employed to monitor the formation of active radicals. When DMPO (a spin-trapping reagent for·OH and O_2^-) was added to the reaction systems, no signal of DMPO-·O_2^- and DMPO-·OH adducts can be detected in the dark (Figure 11), suggesting that negligible OH and·O_2^- radical concentrations were present in the solution. However, under the visible light irradiation, both pristine Bi_2WO_6 and CuS/Bi_2WO_6 heterostructure can produce ESR signals (Figure 11). The characteristic signals of DMPO-·OH with a four-line ESR signal, relative intensities of 1:2:2:1, and $\alpha_H = \alpha_N = 1.5$ mT (Figure 11a) were observed [43,44]. Similarly, a doublet of triplets ESR signal with relative intensities of 1:1:1:1 characteristic signals of DMPO-·O_2^- (Figure 11b) was also observed [45,46]. However, it is worth noting that the coupling constants of DMPO-·O_2^- adduct are $a_H = 0.92$ mT, $a_N = 1.4$ mT, respectively. The value of a_H does not match with the normal value, which may be ascribed to the effects of the solution environment such as pH and solvent. According to the literature reported and our experimental result, the doublet of triplets ESR signal was assigned to DMPO-·O_2^- adduct rather than those centerd on hetero atoms such as O or S [47,48]. Furthermore, compared to pristine Bi_2WO_6, the highly intensive signals were observed for·OH and·O_2^- adducts in the 0.1% CuS/Bi_2WO_6 heterostructure, indicating that CuS/Bi_2WO_6 heterostructure can

generate abundant ·OH and $\cdot O_2^-$ in the presence of visible light and H_2O_2, which is conducive to the degradation of pollutants.

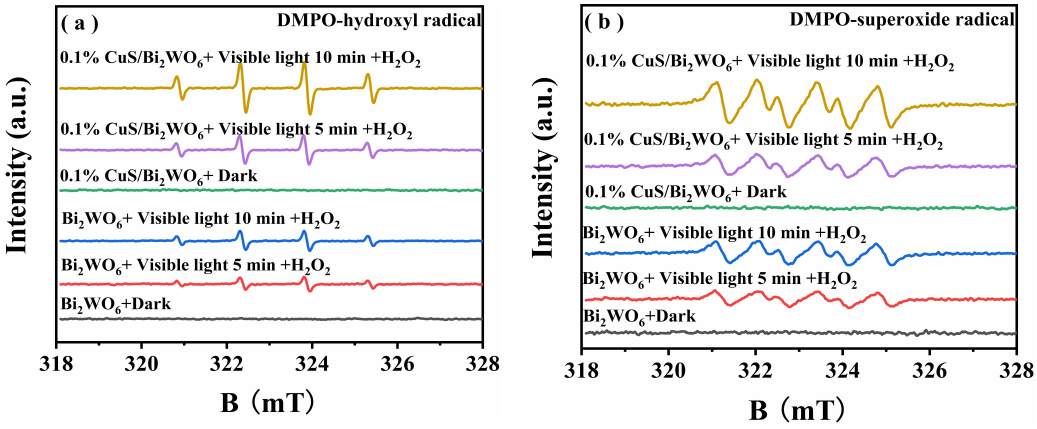

Figure 11. DMPO spin-trapping ESR spectra of Bi_2WO_6 and 0.1% CuS/Bi_2WO_6 heterostructure for (**a**) DMPO-·OH in aqueous dispersion and (**b**) DMPO-$\cdot O_2^-$ in methanol dispersion in the dark or under visible light irradiation and in the presence of H_2O_2, respectively.

The band structure of CuS/Bi_2WO_6 heterostructure was studied by Tauc plots and XPS valence band spectrum analysis. The measured band gap diagram shows that Bi_2WO_6 and CuS, correspond to band gap energies of 2.65 eV and 1.54 eV according to the equation of Kubelka–Munk function, respectively [49], as shown in Figure 12a,b. In addition, according to the intercept with X axis obtained from XPS results, the position of valence band of the material is further determined, indicating that valence band (VB) of Bi_2WO_6 and CuS are 2.24 and 1.46 V, respectively (Figure 12c,d). Therefore, following the empirical equation: $E_{CB} = E_{VB} - E_g$, the conduction band minimum (CBM) of Bi_2WO_6 and CuS are confirmed to be −0.41 and −0.08 V, respectively.

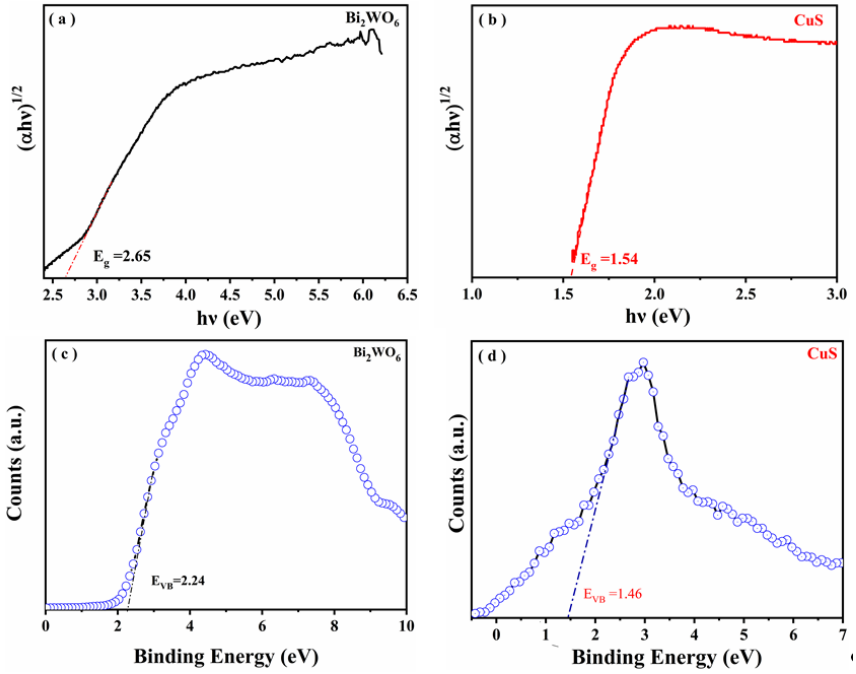

Figure 12. Tauc plots of $(\alpha h\nu)^{1/2}$ vs. hν for the samples Bi_2WO_6 (**a**) and CuS (**b**) and XPS valence band spectra of Bi_2WO_6 (**c**) and CuS (**d**).

In order to further investigate the role of CuS/Bi_2WO_6 heterostructures in photo-Fenton catalysis system, the enhancement mechanism of photo-Fenton activity is discussed, and the schematic diagram is shown in Figure 13a,b. Due to the n-type nature of Bi_2WO_6 and p-type nature of CuS, the Fermi levels of Bi_2WO_6 and CuS are located nearer to the CBM and VBM, respectively. Upon contact between Bi_2WO_6 and CuS, due to Fermi level equilibrium the energy level of CuS is upshifted and Bi_2WO_6 is downshifted leading to the formation of p-n heterojunction [41]. The p-n junction also led to the generation of an internal electric field where the CuS region is negatively charged and the Bi_2WO_6 region is positively charged. This internal field is responsible for efficient separation of the charge carriers. When irradiated with light, both Bi_2WO_6 and CuS are capable of absorbing visible light photons to produce e^-/h^+ pairs. Due to favorable band alignment, the photogenerated electrons can migrate from the CB of CuS to Bi_2WO_6, whereas the migration of holes can take place in reverse direction in the VB of both semiconductor components. This cyclic movement of photogenerated carriers is characteristic of a type-II p-n heterojunction, which leads to their efficient space separation. In the heterogeneous visible light photo-Fenton system constructed in this experiment, the active species involved in the oxidative degradation of organic pollutants mainly include photogenerated holes, O_2^- and ·OH radical.

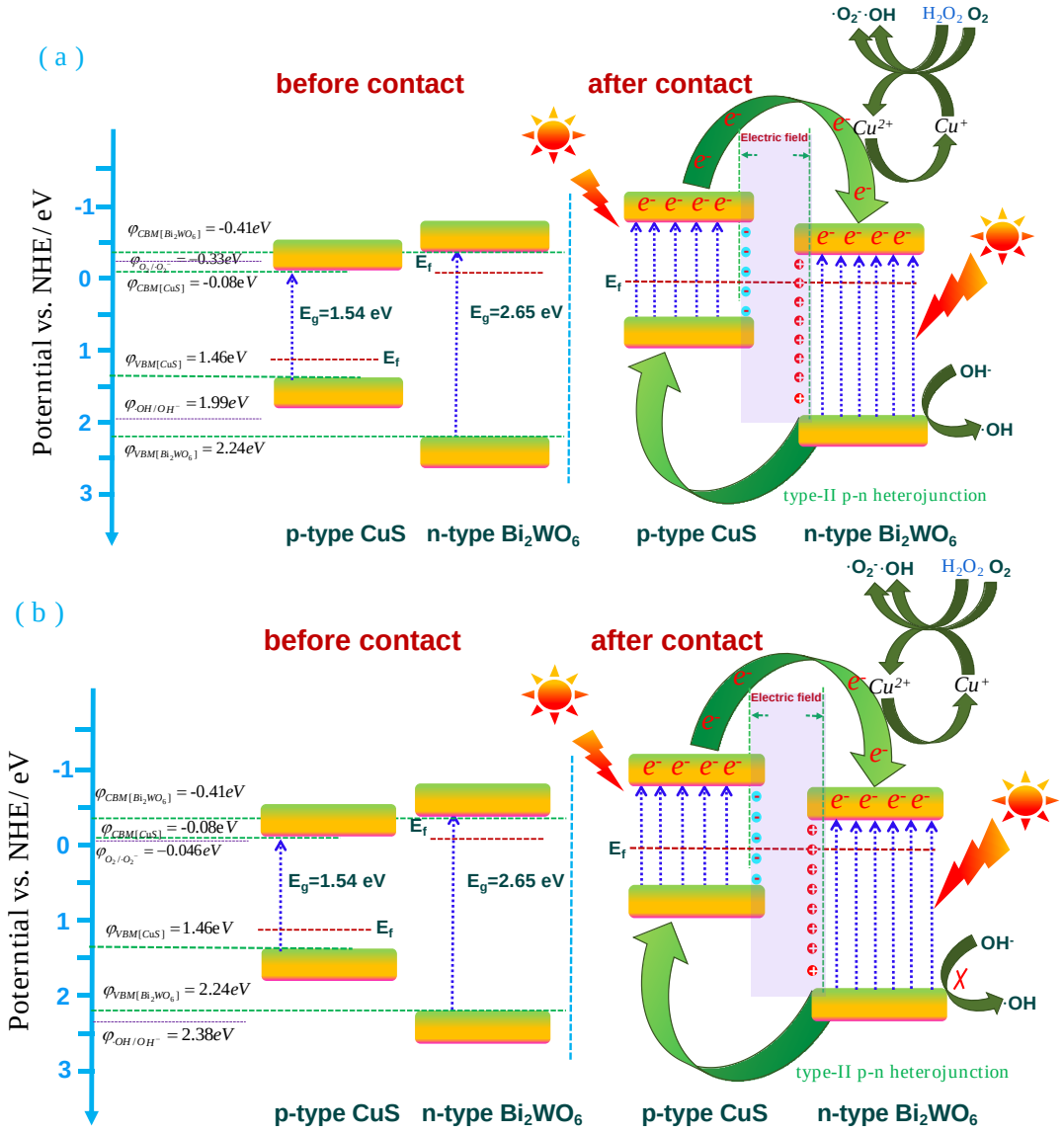

Figure 13. (**a**) The possible photocatalytic and photo-Fenton catalytic mechanism of CuS/Bi_2WO_6 heterostructures for degradation of RhB and (**b**) TC-HCl under visible light irradiation.

When visible light irradiated on the surface of the CuS/Bi_2WO_6 heterostructure, electrons on the Bi_2WO_6 valence band were excited to the conduction band (Equation (1)). Both in the process of degrading RhB and TC-HCl, some electrons in the CB of Bi_2WO_6 could reduce O_2 into $\cdot O_2^-$ because the CB potential of Bi_2WO_6 (−0.41 eV vs. NHE) was more negative than $O_2/\cdot O_2^-$ potential (−0.33 or −0.046 eV vs. NHE) (Figure 13a,b; Equation (2)). The other electrons could transfer to the surface of CuS to react with H_2O_2 to generate ·OH via the photo-Fenton reaction (Equations (4)–(7)), while the photogenerated holes left on the valence band of Bi_2WO_6 could directly degrade RhB and TC-HCl or react with OH^- to generate ·OH (Equation (3)). During the degrading of RhB, the VB holes of Bi_2WO_6 could oxidize OH^- into OH because the VB potential of Bi_2WO_6 (2.24 eV vs. NHE) was more positive than that of $\cdot OH/OH^-$ potential (1.99 eV vs. NHE) (Figure 13a), but could not oxidize OH^- into ·OH during the degradation of TC-HCl because the VB potential of Bi_2WO_6 (2.24 eV vs. NHE) was more negative than $\cdot OH/OH^-$ potential (2.38 eV vs. NHE) (Figure 13b). This resulted in a heterogeneous photo-Fenton process to degrade the organic pollutants via the generated active species (Equation (8)). Possible reactions are described below:

Photocatalysis:

$$CuS(Cu^{II})/Bi_2WO_6 \rightarrow CuS/Bi_2WO_6(h^+ + e^-) \quad (1)$$

$$H_2O_2 + CuS/Bi_2WO_6(e^-) \rightarrow \cdot OH\ O_2 + e^- \rightarrow \cdot O_2^- \quad (2)$$

$$CuS/Bi_2WO_6(h^+) + OH^- \rightarrow \cdot OH \quad (3)$$

Fenton reaction:

$$\equiv Cu^{II}S/Bi_2WO_6 + H_2O_2 \rightarrow H_2O_2 \equiv Cu^{II}S/Bi_2WO_6 \quad (4)$$

$$H_2O_2 \equiv Cu^{II}S/Bi_2WO_6 \rightarrow \equiv Cu^{I}S/Bi_2WO_6 + HO_2 + H^+ \quad (5)$$

$$\equiv Cu^{II}S/Bi_2WO_6 + \cdot HO_2 \rightarrow \equiv Cu^{I}S/Bi_2WO_6 + O_2 + H^+ \quad (6)$$

$$\equiv Cu^{I}S/Bi_2WO_6 + H_2O_2 \rightarrow \equiv Cu^{II}S/Bi_2WO_6 + \cdot OH + OH^- \quad (7)$$

$$\text{Organic pollutants} + \cdot O_2^-/\cdot OH/h^+ \rightarrow \ldots \rightarrow CO_2 + H_2O + \ldots \quad (8)$$

4. Conclusions

In summary, we have developed a simple in situ assembly strategy to construct the two-dimensional (2D) in-plane CuS/Bi_2WO_6 sheet-on-sheet p-n heterostructures and used as photo-Fenton catalysts. A series of techniques were employed to characterize the physical and chemical properties of as-synthesized CuS/Bi_2WO_6 heterostructures. Photo-Fenton catalytic treatment of organic pollutants was successfully achieved by employing CuS/Bi_2WO_6 heterostructures as photocatalysts in the presence of H_2O_2. Photo-Fenton catalytic activity and stability can be significantly promoted by assembling CuS nanosheets on Bi_2WO_6 nanosheets. The excellent photo-Fenton catalytic performance can be attributed to the high-efficiency charge separation and migration of CuS/Bi_2WO_6 p-n heterostructures. The photo-Fenton reaction of CuS on the surface of the heterogeneous catalyst with H_2O_2 produces a large number of $\cdot O_2^-$ and ·OH, which are responsible for the degradation of the organic pollutants. The effects of different factors such as H_2O_2 concentration, catalyst dosage, and initial pH value on TC-HCl degradation were systematically investigated, and the enhanced catalytic oxidation mechanism of 2D/2D CuS/Bi_2WO_6 p-n heterogeneous photo-Fenton system was also elucidated. The present work offers a simple strategy to construct 2D in-plane heterostructures with efficient photo-generated electron–hole separation and high stability, and can be used for wastewater purification via photo-Fenton reaction.

Author Contributions: L.G. designed the experiments and wrote the paper; K.Z. wrote the paper; X.H. and Q.Z. performed the experiments and analyzed the data; D.W. and F.F. designed the experiments. All authors commented and approved the final manuscript.

Funding: This work was financially supported by the National Natural Science Foundation of China (No. 21663030, 21666039) and the Open Project of State Key Laboratory of Organic–Inorganic Composites Beijing Key Laboratory, Beijing University of Chemical Technology Beijing (No. oic-201901009) and the Project of Science & Technology Office of Shaanxi Province (No. 2018TSCXL-NY-02-01, 2015SF291, 2013K11-08, 2013SZS20-P01) and the Project of Yan'an Science and Technology Bureau (No. 2018KG-04) and Graduate Innovation Project of Yan'an University.

Conflicts of Interest: The authors declare no conflict of interest.

References

1. Wang, M.; Tan, G.Q.; Zhang, D.; Li, B.; Lv, L.; Wang, Y.; Ren, H.J.; Zhang, X.L.; Xia, A.; Liu, Y. Defect-mediated Z-scheme $BiO_{2-x}/Bi_2O_{2.75}$ Photocatalyst for Full Spectrum Solar-Driven Organic Dyes Degradation. *Appl. Catal. B: Environ.* **2019**, *254*, 98–112. [CrossRef]
2. Tran, N.H.; Reinhard, M.; Gin, K.Y.-H. Occurrence and Fate of Emerging Contaminants in Municipal Wastewater Treatment Plants from Different Geographical Regions-A Review. *Water Res.* **2018**, *133*, 182–207. [CrossRef] [PubMed]
3. Jourshabani, M.; Shariatinia, Z.; Badiei, A. In Situ Fabrication of SnO_2/S-doped g-C_3N_4 Nanocomposites and Improved Visible Light Driven Photodegradation of Methylene Blue. *J. Mol. Liquid* **2017**, *248*, 688–702. [CrossRef]
4. Pereira, J.H.O.S.; Vilar, V.J.P.; Borges, M.T.; González, O.; Esplugas, S.; Boaventura, R.A.R. Photocatalytic Degradation of Oxytetracycline using TiO_2 under Natural and Simulated Solar Radiation. *Sol. Energy* **2011**, *85*, 2732–2740. [CrossRef]
5. Daghrir, R.; Drogui, P. Tetracycline Antibiotics in the Environment: A Review. *Environ. Chem. Lett.* **2013**, *11*, 209–227. [CrossRef]
6. Feng, B.; Wu, Z.Y.; Liu, J.S.; Zhu, K.J.; Li, Z.Q.; Jin, X.; Hou, Y.D.; Xi, Q.Y.; Cong, M.Q.; Liu, P.C.; et al. Combination of Ultrafast Dye-Sensitized-Assisted Electron Transfer Process and Novel Z-Scheme System: AgBr Nanoparticles Interspersed MoO_3 Nanobelts for Enhancing Photocatalytic Performance of RhB. *Appl. Catal. B: Environ.* **2017**, *206*, 242–251. [CrossRef]
7. Shao, B.B.; Liu, X.J.; Liu, Z.F.; Zeng, G.M.; Liang, Q.H.; Liang, C.; Cheng, Y.; Zhang, W.; Liu, Y.; Gong, S.X. A Novel Double Z-Scheme Photocatalyst $Ag_3PO_4/Bi_2S_3/Bi_2O_3$ with Enhanced Visible-Light Photocatalytic Performance for Antibiotic Degradation. *Chem. Eng. J.* **2019**, *368*, 730–745. [CrossRef]
8. Andreozzi, R.; Caprio, V.; Insola, A.; Marotta, R. Advanced Oxidation Processes (AOP) for Water Purification and Recovery. *Catal. Today* **1999**, *53*, 51–59. [CrossRef]
9. Giannakis, S.; Liu, S.T.; Carratalà, A.; Rtimi, S.; Bensimon, M.; Pulgarin, C. Effect of Fe(II)/Fe(III) Species, pH, Irradiance and Bacterial Presence on Viral Inactivation in Wastewater by the Photo-Fenton Process: Kinetic Modeling and Mechanistic Interpretation. *Appl. Catal. B: Environ.* **2017**, *204*, 156–166. [CrossRef]
10. Li, W.H.; Wu, X.F.; Li, S.D.; Tang, W.X.; Chen, Y.F. Magnetic Porous Fe_3O_4/Carbon Octahedra Derived from Iron-based Metal-Organic Framework as Heterogeneous Fenton-like Catalyst. *Appl. Surf. Sci.* **2018**, *436*, 252–262. [CrossRef]
11. Nogueira, R.F.P.; Oliveira, M.C.; Paterlini, W.C. Simple and Fast Spectrophotometric Determination of H_2O_2 in Photo-Fenton Reactions Using Metavanadate. *Talanta* **2005**, *66*, 86–91. [CrossRef]
12. Jiang, J.J.; Gao, J.Y.; Li, T.R.; Chen, Y.F.; Wu, Q.N.; Xie, T.T.; Lin, Y.H.; Dong, S.S. Visible-Light-Driven Photo-Fenton Reaction with α-Fe_2O_3/BiOI at Near Neutral pH: Boosted Photogenerated Charge Separation, Optimum Operating Parameters and Mechanism Insight. *J. Colloid Interface Sci.* **2019**, *554*, 531–543. [CrossRef]
13. Jiang, L.L.; Zhang, L.; Cui, C.; Zhang, J.; Liu, G.D.; Song, J.J. Efficient Degradation of Phenol using Sn^{4+} Doped FeOCl as Photo-Fenton Catalyst. *Mater. Lett.* **2019**, *240*, 30–34. [CrossRef]
14. Zhang, L.; Wu, B.D.; Zhang, G.Y.; Gan, Y.H.; Zhang, S.J. Enhanced Decomplexation of Cu(II)-EDTA: The Role of Acetylacetone in Cu-Mediated Photo-Fenton Reactions. *Chem. Eng. J.* **2019**, *358*, 1218–1226. [CrossRef]
15. Xu, Z.; Shan, C.; Xie, B.H.; Liu, Y.; Pan, B.C. Decomplexation of Cu(II)-EDTA by UV/Persulfate and UV/H_2O_2: Efficiency and Mechanism. *Appl. Catal. B: Environ.* **2017**, *200*, 439–447. [CrossRef]
16. Xu, T.Y.; Zhu, R.L.; Zhu, G.Q.; Zhu, J.X.; Liang, X.L.; Zhu, Y.P.; He, H.P. Mechanisms for the Enhanced Photo-Fenton Activity of Ferrihydrite Modified with $BiVO_4$ at Neutral pH. *Appl. Catal. B: Environ.* **2017**, *212*, 50–58. [CrossRef]

17. Zhu, Y.P.; Zhu, R.L.; Yan, L.X.; Fu, H.Y.; Xi, Y.F.; Zhou, H.J.; Zhu, G.Q.; He, H.P. Visible-Light Ag/AgBr/Ferrihydrite Catalyst with Enhanced Heterogeneous Photo-Fenton Reactivity via Electron Transfer From Ag/AgBr to Ferrihydrite. *Appl. Catal. B: Environ.* **2018**, *239*, 280–289. [CrossRef]
18. Qian, X.F.; Wu, Y.W.; Kan, M.; Fang, M.Y.; Yue, D.T.; Zeng, J.; Zhao, Y.X. FeOOH Quantum Dots Coupled g-C_3N_4 for Visible Light Driving Photo-Fenton Degradation of Organic Pollutants. *Appl. Catal. B: Environ.* **2018**, *237*, 513–520. [CrossRef]
19. Jiang, Z.Y.; Wang, L.Z.; Lei, J.Y.; Liu, Y.D.; Zhang, J.L. Photo-Fenton Degradation of Phenol by CdS/rGO/Fe^{2+} at Natural pH with In Situ-generated H_2O_2. *Appl. Catal. B: Environ.* **2019**, *241*, 367–374. [CrossRef]
20. Soltani, T.; Lee, B.K. Enhanced Formation of Sulfate Radicals by Metal-Doped $BiFeO_3$ under Visible Light for Improving Photo-Fenton Catalytic Degradation of 2-Chlorophenol. *Chem. Eng. J.* **2017**, *313*, 1258–1268. [CrossRef]
21. Hu, S.P.; Xu, C.Y.; Zhen, L. Solvothermal Synthesis of Bi_2WO_6 Hollow Structures with Excellent Visible-Light Photocatalytic Properties. *Mater. Lett.* **2013**, *95*, 117–120. [CrossRef]
22. Sheng, J.Y.; Li, X.J.; Xu, Y.M. Generation of H_2O_2 and OH Radicals on Bi_2WO_6 for Phenol Degradation under Visible Light. *ACS Catal.* **2014**, *4*, 732–737. [CrossRef]
23. Wang, D.J.; Guo, L.; Zhen, Y.Z.; Yue, L.L.; Xue, G.L.; Fu, F. AgBr Quantum Dots Decorated Mesoporous Bi_2WO_6 Architectures with Enhanced Photocatalytic Activities for Methylene Blue. *J. Mater. Chem. A* **2014**, *2*, 11716–11727. [CrossRef]
24. Zhang, Z.J.; Wang, W.Z.; Wang, L.; Sun, S.M. Enhancement of Visible-Light Photocatalysis by Coupling with Narrow-Band-Gap Semiconductor: A Case Study on Bi_2S_3/Bi_2WO_6. *ACS Appl. Mater. Interfaces* **2012**, *4*, 593–597. [CrossRef]
25. Zhang, L.; Wang, W.Z.; Shang, M.; Sun, S.M.; Xu, J.H. Bi_2WO_6@Carbon/Fe_3O_4 Microspheres: Preparation, Growth Mechanism and Application in Water Treatment. *J. Hazard. Mater.* **2009**, *172*, 1193–1197. [CrossRef]
26. Xiao, Q.; Zhang, J.; Xiao, C.; Tan, X.K. Photocatalytic Degradation of Methylene Blue over Co_3O_4/Bi_2WO_6 Composite under Visible Light Irradiation. *Catal. Commun.* **2008**, *9*, 1247–1253. [CrossRef]
27. Shan, G.Q.; Fu, Y.; Chu, X.L.; Chang, C.; Zhu, L.Y. Highly Active Magnetic Bismuth Tungstate/Magnetite Composite under Visible Light Irradiation in the Presence of Hydrogen Peroxide. *J. Colloid Interface Sci.* **2015**, *444*, 123–131. [CrossRef]
28. Gao, L.G.; Du, J.W.; Ma, T.L. Cysteine-Assisted Synthesis of CuS-TiO_2 Composites with Enhanced Photocatalytic Activity. *Ceram. Int.* **2017**, *43*, 9559–9563. [CrossRef]
29. Cai, Z.L.; Zhou, Y.M.; Ma, S.S.; Li, S.W.; Yang, H.Y.; Zhao, S.; Zhong, X.; Wu, W.T. Enhanced Visible Light Photocatalytic Performance of g-C_3N_4/CuS *p-n* Heterojunctions for Degradation of Organic Dyes. *J. Photoch. Photobio. A* **2017**, *348*, 168–178. [CrossRef]
30. Bhoi, Y.P.; Mishra, B.G. Photocatalytic Degradation of Alachlor using Type-II CuS/$BiFeO_3$ Heterojunctions as Novel Photocatalyst under Visible Light Irradiation. *Chem. Eng. J.* **2018**, *344*, 391–401. [CrossRef]
31. Bhoi, Y.P.; Behera, C.; Majhi, D.; Equeenuddin, S.M.; Mishra, B.G. Visible Light-Assisted Photocatalytic Mineralization of Diuron Pesticide using Novel type II CuS/$Bi_2W_2O_9$ Heterojunctions with a Hierarchical Microspherical Structure. *New J. Chem.* **2018**, *42*, 281–292. [CrossRef]
32. Zhao, W.; Liang, C.; Wang, B.B.; Xing, S.T. Enhanced Photocatalytic and Fenton-Like Performance of CuO_x-Decorated $ZnFe_2O_4$. *ACS Appl. Mater. Interfaces* **2017**, *9*, 41927–41936. [CrossRef]
33. Zhou, Y.G.; Zhang, Y.F.; Lin, M.S.; Long, J.L.; Zhang, Z.Z.; Lin, H.X.; Wu, J.C.S.; Wang, X.X. Monolayered Bi_2WO_6 Nanosheets Mimicking Heterojunction Interface with Open Surfaces for Photocatalysis. *Nat. Commun.* **2015**, *6*, 8340. [CrossRef]
34. Qian, X.F.; Yue, D.T.; Tian, Z.Y.; Ren, M.; Zhu, Y.; Kan, M.; Zhang, T.Y.; Zhao, Y.X. Carbon Quantum Dots Decorated Bi_2WO_6 Nanocomposite with Enhanced Photocatalytic Oxidation Activity for VOCs. *Appl. Catal. B: Environ.* **2016**, *193*, 16–21. [CrossRef]
35. Wang, J.J.; Tang, L.; Zeng, G.M.; Deng, Y.C.; Dong, H.R.; Liu, Y.N.; Wang, L.L.; Peng, B.; Zhang, C.; Chen, F. 0D/2D Interface Engineering of Carbon Quantum Dots Modified Bi_2WO_6 Ultrathin Nanosheets with Enhanced Photoactivity for Full Spectrum Light Utilization and Mechanism Insight. *Appl. Catal. B: Environ.* **2018**, *222*, 115–123. [CrossRef]
36. Wang, Y.Y.; Jiang, W.J.; Luo, W.J.; Chen, X.J.; Zhu, Y.F. Ultrathin Nanosheets g-C_3N_4@Bi_2WO_6 Core-shell Structure via Low Temperature Reassembled Strategy to Promote Photocatalytic Activity. *Appl. Catal. B: Environ.* **2018**, *237*, 633–640. [CrossRef]

37. Chen, S.B.; Lin, X.; Zhou, W.Y.; Zhang, S.S.; Fang, Y.P. Carbon-Coated Cu-TiO_2 Nanocomposite with Enhanced Photostability and Photocatalytic Activity. *Appl. Surf. Sci.* **2019**, *466*, 254–261. [CrossRef]
38. Wang, X.T.; Li, Y.; Zhang, X.Q.; Li, J.F.; Luo, Y.N.; Wang, C.W. Fabrication of a Magnetically Separable $Cu_2ZnSnS_4/ZnFe_2O_4$ *p-n* Heterostructured Nano-Photocatalyst for Synergistic Enhancement of Photocatalytic Activity Combining with Photo-Fenton Reaction. *Appl. Surf. Sci.* **2019**, *479*, 86–95. [CrossRef]
39. Ruan, X.W.; Hu, H.; Che, H.N.; Jiang, E.H.; Zhang, X.X.; Liu, C.B.; Che, G.B. A Visible-Light-Driven Z-Scheme $CdS/Bi_{12}GeO_{20}$ Heterostructure with Enhanced Photocatalytic Degradation of Various Organics and the Reduction of Aqueous Cr(VI). *J. Colloid Interface Sci.* **2019**, *543*, 317–327. [CrossRef]
40. Yang, J.; Wang, X.H.; Chen, Y.M.; Dai, J.; Sun, S.H. Enhanced Photocatalytic Activities of Visible-Light Driven Green Synthesis in Water and Environmental Remediation on Au/Bi_2WO_6 Hybrid Nanostructures. *RSC Adv.* **2015**, *5*, 9771–9782. [CrossRef]
41. Das, K.; Majhi, D.; Bhoi, Y.P.; Mishra, B.G. Combustion Synthesis, Characterization and Photocatalytic Application of $CuS/Bi_4Ti_3O_{12}$ *p-n* Heterojunction Materials towards Efficient Degradation of 2-Methyl-4-Chlorophenoxyacetic Acid Herbicide under Visible Light. *Chem. Eng. J.* **2019**, *362*, 588–599. [CrossRef]
42. Yu, X.D.; Lin, X.C.; Feng, W.; Li, W.G. Effective Removal of Tetracycline by Using Bio-Templated Synthesis of TiO_2/Fe_3O_4 Heterojunctions as a UV-Fenton Catalyst. *Catal. Lett.* **2019**, *149*, 552–560. [CrossRef]
43. Wang, K.; Li, Y.; Zhang, G.K.; Li, J.; Wu, X.Y. 0D Bi Nanodots/2D Bi_3NbO_7 Nanosheets Heterojunctions for Efficient Visible Light Photocatalytic Degradation of Antibiotics: Enhanced Molecular Oxygen Activation and Mechanism Insight. *Appl. Catal. B: Environ.* **2019**, *240*, 39–49. [CrossRef]
44. Yang, M.; Yang, Q.; Zhong, J.B.; Huang, S.T.; Li, J.Z.; Song, J.B.; Burda, C. Enhanced Photocatalytic Performance of Ag_2O/BiOF Composite Photocatalysts Originating from Efficient Interfacial Charge Separation. *Appl. Surf. Sci.* **2017**, *416*, 666–671. [CrossRef]
45. Ma, D.M.; Zhong, J.B.; Li, J.Z.; Burda, C.; Duan, R. Preparation and Photocatalytic Performance of MWCNTs/BiOCl: Evidence for the Superoxide Radical Participation in the Degradation Mechanism of phenol. *Appl. Surf. Sci.* **2019**, *480*, 395–403. [CrossRef]
46. Yang, J.; Dai, J.; Chen, C.C.; Zhao, J.C. Effects of Hydroxyl Radicals and Oxygen Species on the 4-Chlorophenol Degradation by Photoelectrocatalytic Reactions with TiO_2-Film Electrodes. *J. Photochem. Photobio. A: Chem.* **2009**, *208*, 66–77. [CrossRef]
47. Cai, T.; Liu, Y.T.; Wang, L.L.; Dong, W.Y.; Chen, H.; Zeng, W.G.; Xia, X.N.; Zeng, G.M. Activation of Persulfate by Photoexcited Dye for Antibiotic Degradation: Radical and Nonradical Reactions. *Chem. Eng. J.*. [CrossRef]
48. Liu, L.D.; Wang, Y.; Liu, Q.; Wang, W.J.; Duan, L.; Yang, X.; Yi, S.X.; Xue, X.T.; Zhang, J.W. Activation Peroxydisulfate by Morphology-Dependent NiO Catalysts: Structural Origin of Different Catalytic Properties. *Appl. Catal. B: Environ.*. [CrossRef]
49. Fu, F.; Shen, H.D.; Sun, X.; Xue, W.W.; Shoneyec, A.; Ma, J.N.; Luo, L.; Wang, D.J.; Wang, J.G.; Tang, J.W. Synergistic Effect of Surface Oxygen Vacancies and Interfacial Charge Transfer on $Fe(III)/Bi_2MoO_6$ for Efficient Photocatalysis. *Appl. Catal. B: Environ.* **2019**, *247*, 150–162. [CrossRef]